All-electric spin pumping in quantum channels with a single finger-gate capacitor

L. Y. Wang
Department of Physics, Fu Jen Catholic University, New Taipei City 24205, Taiwan

C. S. Chu
Department of Electrophysics, National Chiao Tung University, Hsinchu 30010, Taiwan

(Received 18 October 2016; revised manuscript received 17 January 2017; published 7 February 2017)

In this paper, we show that a single finger-gate capacitor (FGC) can generate pure spin pumping in a quantum channel (QC). Two dynamic fields, ac spin-orbit interaction and ac potential energy, both induced by the FGC onto the QC, are the agents driving the spin pumping. Smooth spatial profiles of the two ac fields are taken into account both perturbatively and full numerically for the nonadiabatic spin pumping. Our perturbative approach reveals that the spin-pumping mechanism is resonant sideband processes associated with simultaneous coupling of the two ac fields with traversing carriers. Full sideband-process treatment is carried out numerically by a time-dependent scattering matrix method. The same spin-pumping mechanism holds also for the case of a single finger-gated QC, albeit with smaller pumping amplitudes.

DOI: 10.1103/PhysRevB.95.075406

I. INTRODUCTION

Spintronics aim to generate, manipulate, and detect spin current for both application and fundamental arenas [1,2]. Spin current injection in metallic heterostructures involving ferromagnetic components is well established, and more recent developments include, among others, spin pumping at a ferromagnetic/paramagnetic interface, where a precessing magnetization on the ferromagnetic side induces spin currents on the paramagnetic side [3–5]. Spin current injection at a ferromagnetic/semiconducting interface, however, remains a challenge [6,7] subjecting to further advancement in interface physics and technology. In the presence of Tesla-scale magnetic fields, spin current injection in all-semiconductor nanostructures was demonstrated [8–10], where quantum point contacts (QPC) transmit spin-polarized currents in the presence of the magnetic field. External magnetic field was also invoked for spin pumping driven by electric dipole spin resonance in all-semiconductor devices [11,12], when gate-induced oscillating electric fields in parallel with a static magnetic field are both in plane [11] or out of plane [12] to the same device region where spin-orbit interaction (SOI) [13–17] is at work.

At the heart of spintronics, however, is all-electric spin current generation in all-semiconductor devices [18–32], where no ferromagnetic materials and magnetic fields are involved. Configurations with two spatially separated time-modulated regions for spin pumping were proposed. These were adiabatic quantum (charge) pumping [33–36] configurations extended, for instance, to include SOI to a mesoscopic quantum dot (QD) acted upon by two dot-confinement-modulating gates [18], to replace one of the two potential-modulating gates in a quantum channel (QC) by a SOI-modulating gate [19], or to replace, also in a QC, the pair of potential-modulating gates by two SOI-modulating finger-gate capacitors (FGC) oriented orthogonally to each other [26]. The proposals were prompted by the recently demonstrated electric modulation of the Rashba SOI in structure inversion asymmetric quantum wells [37,38]. Other adiabatic spin-pumping proposals involve time-modulating SOI quantum dots in both their energy levels and the coupling between the QD and the leads [27,29].

Aside from pumping, spin-polarized current schemes for QC of high intrinsic SOI had been studied. It is by imposing a highly asymmetric lateral QC confinement [25], a potential barrier located at and along the QC central line [30], or a transverse lead, as in a mesoscopic spin Hall effect configuration, for spin current extraction when a charge current passes through the source and drain leads [31]. These spin-polarized current schemes, however, operate with a finite source-drain bias. We thus opt to consider spin pumping, which has the added advantage of *zero* source-drain bias. Our focus is upon the simplest gated QC, namely, a single finger-gated QC.

Consensus has not been reached on whether a single finger-gated QC generates spin pumping. On the one hand, nonadiabatic spin pumping for one ac gate-induced field case had been demonstrated [21,23]. The ac field is a SOI field, which is gate induced and was assumed to have a stepwise spatial profile. Besides, the QC has uniform and static SOI, which is Rashba SOI in Ref. [21], and Rashba and Dresselhaus SOIs in Ref. [23]. The nonadiabatic spin-pumping results have left concerns about the simplified profile for the ac SOI field [12], and the possible effects of the ac gate-induced potential field, which was not considered in [21,23]. On the other hand, spin pumping was not found in two ac gate-induced fields case [12]. The ac fields are the gate-induced SOI and potential fields; both are of smooth spatial profiles. Besides, the QC has static gate-induced SOI and potential fields (both having smooth spatial profiles), but no uniform static SOI. Including only up to ± 1 sidebands in their calculations, no spin pumping was found [12]. Thus, a comprehensive study is needed to fully explore and to understand the spin-pumping nature in a single finger-gated QC. Issues including spatial profiles of the ac fields, the case for two ac fields, and many sideband effects need to be studied in detail.

On the spatial profile issue, we show that a single finger-gated QC can generate spin pumping, regardless of the spatial profiles of the gate-induced ac fields. To obtain a transparent physical picture, we develop a time-dependent perturbation theory that has incorporated the smooth induced-field-profile feature. Expressions for spin-dependent transmissions are obtained, up to the lowest (second) order in the gate bias.

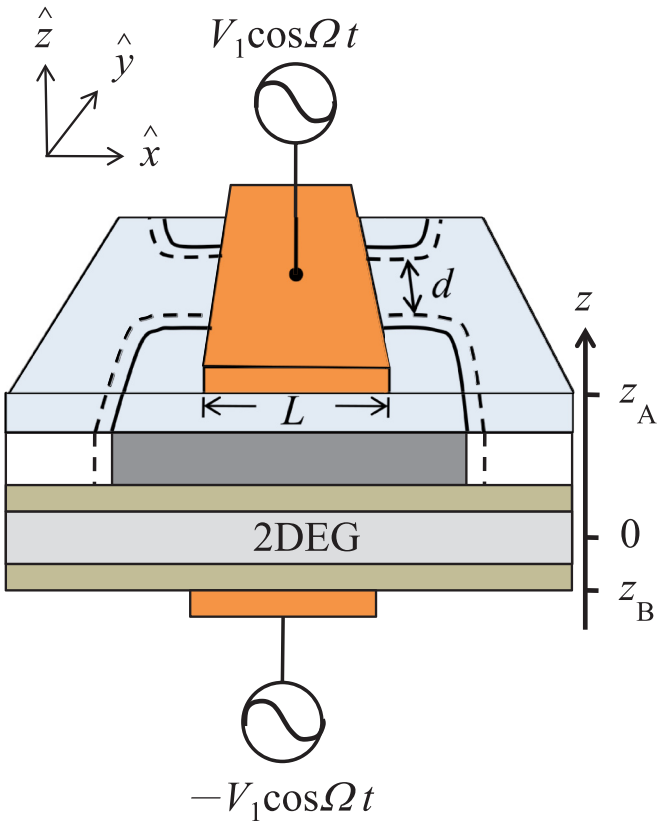

FIG. 1. Schematic illustration of the finger-gate-capacitor quantum channel. The quantum channel, depicted by the dashed lines (channel width d), is formed in the two-dimensional electron gas (2DEG) layer due to split-gate (dark gray colored cross section traced by the dashed lines) biases. The single finger-gate capacitor consists of an aligned gate pair (orange) of longitudinal length L at $z = z_B$ and $z = z_A$. Indicated also are the ac biases of the finger-gate capacitor for the spin pumping.

Higher-order treatment is found to become important when states near the subband bottom are involved due to resonant inelastic processes. We thus perform also a full high-order numerical calculation by extending a time-dependent scattering matrix method [39] to the present problem. The QCs that we consider have gate-induced ac SOI and potential energy fields but no static SOI fields. Nonzero difference in the spin-dependent transmissions leads to spin pumping.

The perturbation expression that we obtain for the transmission difference has the induced-field profiles entered in the form of spatial integrals. This in turn shows that variations in the spatial profiles should only have quantitative rather than qualitative effects on the spin-pumping characteristics. We note that, in this work, a single finger-gate-capacitor configuration is considered instead of a single finger-gate configuration. The finger-gate-capacitor configuration provides an additional knob for the tuning of the relative strengths between the induced SOI and the potential energy fields. It is by way of symmetric or asymmetric sandwiching of the QC by the finger-gate capacitor, as is shown in Fig. 1.

Our perturbation results also exhibit clearly the mechanisms for the spin pumping. In the absence of a static and uniform SOI, the spin pumping is resulted from simultaneous coupling of the ac gate-induced SOI and potential energy fields to the traversing electrons. In the presence of a static and uniform SOI, additional spin-pumping mechanism arises from simultaneous coupling of the ac gate-induced SOI and the static SOI with the electrons.

We have shown that these spin-pumping mechanisms and the resonant inelastic nature in a QC together contribute appreciably to spin pumping. The inelastic processes are sideband processes where the traversing electrons have their energy μ changes to $\mu \pm n\hbar\Omega$, where Ω is the frequency of the ac gate bias, n is an integral sideband index, and μ is measured from the subband bottom. The sideband processes become resonant when states around the subband bottom are involved, and the resonant condition is $\mu = n\hbar\Omega$ [21,23,39–41]. It is due to the singular density of states at a QC subband bottom. The resonance typically features a dip structure in the energy dependence of the transmission [21,23,39–41] which, in a way, exhibits the temporal trapping characteristics of the electron by the time-modulated agent [40].

This paper is organized as follows. In Sec. II, we present our time-dependent perturbation method. This serves to illustrate the physical mechanisms of the spin pumping. Time-dependent scattering matrix method is presented in Sec. III. This is for the treatment of general pumping parameters. Numerical results and discussions are presented in Sec. IV, and, finally, presented in Sec. V is our conclusion.

II. PERTURBATION METHOD

This section presents our time-dependent perturbation method that has incorporated the smooth induced-field-profile feature of the ac fields. We have included, for the sake of completeness, a static and uniform Rashba SOI in the QC. The perturbation will treat the static Rashba SOI, the ac SOI, and the ac potential energy fields all on the same footing. The perturbation scheme here provides a framework to treat systematically terms that involve both spatial and time dependencies simultaneously, to extract from the framework useful quantities such as scattering coefficients, and to see explicitly the effects of the density of states from the derived expressions. In particular, the need for higher-order perturbation, as is prompted by the density of states relevant to sideband processes, becomes transparent in our expressions in, for instance, Eq. (24). For simplicity, we consider QC with sufficiently narrow widths such that only the lowest subband is needed for our considerations [12,21–23,26]. The purpose of this section is to show that spin-dependent transmission difference [Eq. (24)] is nonzero for any given incident energy. This finding leads to nonzero net spin pumping, where all incident states with energies below the Fermi energy contribute [Eq. (40)], and is shown numerically in Sec. IV.

The Hamiltonian of the QC is given by

$$H = H_0 + H_{\rm SO}^0 + U(x,t) + H_{\rm SO}(t), \tag{1}$$

where $H_0 = p^2/(2m) + U_c(y)$ with $U_c(y)$ the confinement potential; $H_{\rm SO}^0 = \alpha_0 (\hat{z} \times \boldsymbol{\sigma}) \cdot \boldsymbol{p}$ is the static uniform Rashba SOI [16,17]; and $\boldsymbol{\sigma}$ is the vector of Pauli matrices $(\sigma_x,\sigma_y,\sigma_z)$ for the electron spin. Both electric field $\mathbf{E}(x,t)$ and potential energy $U(x,t)$ are induced from the same ac-biased gate structures (see Fig. 1). The ac SOI term $H_{\rm SO}(t) = \frac{\lambda}{2} \{(\boldsymbol{\sigma} \times \boldsymbol{p}) \cdot$

$\mathbf{E}(x,t) + [\mathbf{E}(x,t) \times \boldsymbol{\sigma}] \cdot \mathbf{p}\}$ [13]. The SOI coupling constants are α_0 and λ. By focusing on one-dimensional QCs where only the lowest subband is involved, SOI terms in H that contain p_y, the transverse momentum, can be neglected. Subsequently, the only spin component that appears in H is σ_y. We then choose the wave function $|\Psi_\eta(x,t)\rangle\,\chi_\eta$ to be spin eigenstates where $\sigma_y \chi_\eta = \eta\,\chi_\eta$ and $\eta = \pm$. The Schrödinger equation becomes

$$H_\eta |\Psi_\eta(x,t)\rangle = i\hbar \frac{\partial}{\partial t} |\Psi_\eta(x,t)\rangle, \tag{2}$$

where

$$H_\eta = \left(\varepsilon_0 - \frac{1}{2} m\alpha_0^2\right) + H_\eta^0 + \frac{\lambda\overline{\eta}}{2}\{E_z(x,t), p_x\} + U(x,t) \tag{3}$$

and

$$H_\eta^0 = \frac{1}{2m}[p_x + m\overline{\eta}\alpha_0]^2. \tag{4}$$

Here, ε_0 is the lowest subband energy, $\overline{\eta} = -\eta$, and the third term in Eq. (3) is an anticommutator. It is convenient that we absorb the constant energy term in Eq. (3) by considering H'_η instead in the following, where

$$H'_\eta = H_\eta - \left(\varepsilon_0 - \tfrac{1}{2} m\alpha_0^2\right). \tag{5}$$

The finger-gate capacitor and the bias, as shown in Fig. 1, generates electric potential $V(x,z,t)$ [12,42], given by

$$V(x,z,t) = V_1 \cos(\Omega t)[\xi(x, z - z_A) - \xi(x, z - z_B)], \tag{6}$$

where

$$\xi(x,z) = \frac{1}{\pi}\left[\tan^{-1}\left(\frac{L/2 + x}{|z|}\right) + \tan^{-1}\left(\frac{L/2 - x}{|z|}\right)\right]. \tag{7}$$

The potential in the vicinity of the QC is uniform in y as long as the length of the finger gate along $\hat{y}$ is much greater than z_A, $|z_B|$, and d. This potential form, given by Eq. (7), is valid in the quasielectrostatic regime, when the relevant wavelength of the ac field, given by $\Lambda = 2\pi c/\Omega$, is much larger than all length scales in the system. For $f = \Omega/(2\pi) =$ 1 THz, the $\Lambda = 300\ \mu$m justifies the choice of the potential form. Here, c is the speed of light. We point out also that $\xi(x,z) = (\phi_L + \phi_R)/\pi$ where ϕ_L (ϕ_R) is the azimuthal angle between the (x,z) point and the line (parallel to $\hat{z}$) passing through the left (right) edge of the gate. The sign convention is that $\phi_L = \phi_R = \pi/2$ at the origin of the x-z plane, and the satisfaction of $\xi(x,z)$ to the Laplace equation is self-evident.

The induced electric field acting upon the QC, located at $z = 0$, is

$$E_z(x,t) = V_1 \cos(\Omega t)\,[\xi'(x,z_A) - \xi'(x,z_B)], \tag{8}$$

where $\xi'(x,z) \equiv \partial\xi/\partial z$. The induced potential energy acting on the QC is $U(x,t) = -eV(x,0,t)$ where $-e$ is an electron charge.

For the following time-dependent perturbation treatment, it is convenient to cast $H'_\eta = H_\eta^0 + H_\eta^{so}(t) + U(x,t)$ and to introduce dimensionless field profile functions $f(x)$ and $g(x)$ for, respectively, the ac SOI and potential energy terms such that

$$H'_\eta = H_\eta^0 + \frac{\alpha_1\overline{\eta}}{2}\cos(\Omega t)\{f(x), p_x\} + U_1 \cos(\Omega t) g(x), \tag{9}$$

with

$$\begin{aligned} f(x) &= h_0[\xi'(x,z_A) - \xi'(x,z_B)], \\ g(x) &= \xi(x,z_A) - \xi(x,z_B), \end{aligned} \tag{10}$$

where $h_0 = z_A + |z_B|$ is the vertical gate separation of the finger-gate capacitor, $\alpha_1 = \lambda V_1/h_0$, and $U_1 = -eV_1$. The form of H'_η as defined in Eqs. (9) and (5) has the time dependence shown explicitly while the SOI coupling constants α_1 and α_0 are in the same dimension.

Starting from Eq. (9) and going to the interaction picture, where $|\Psi_\eta\rangle = e^{-iH_\eta^0 t/\hbar}\,|\psi_\eta\rangle$, we have

$$\begin{aligned} i\hbar\frac{\partial}{\partial t}|\psi_\eta\rangle = {} & \frac{\alpha_1\overline{\eta}}{2}\cos(\Omega t)\, e^{\zeta t}\,\{f_{\rm I}(x,t), p_x\}\,|\psi_\eta\rangle \\ & + U_1 \cos(\Omega t)\, e^{\zeta t}\; g_{\rm I}(x,t)\,|\psi_\eta\rangle, \end{aligned} \tag{11}$$

where $f_{\rm I}(x,t) = e^{iH_\eta^0 t/\hbar} f(x,t) e^{-iH_\eta^0 t/\hbar}$, and $g_{\rm I}(x,t)$ is defined similarly. Adiabatic factors $e^{\zeta t}$ are introduced in Eq. (11) to facilitate our perturbation in the following.

A right-going incident wave $|\psi_\eta^0\rangle = |k_{\eta R}\rangle$ of energy μ satisfies $H_\eta^0|k_{\eta R}\rangle = \mu|k_{\eta R}\rangle$, where $k_{\eta R} = K - m\alpha_0\overline{\eta}/\hbar$, $\mu = \hbar^2K^2/(2m)$, and $\langle x|k_{\eta R}\rangle = e^{ik_{\eta R}x}/\sqrt{L_x}$. Here, L_x is a representative system size along x which we will take $L_x = 1$ in the following for presentation sake.

The first-order correction, in V_1, to the wave function $|\psi_\eta\rangle = |k_{\eta R}\rangle + |\psi_\eta^{(1)}\rangle$ has taken the expansion form

$$\left|\psi_\eta^{(1)}\right\rangle = {\sum_{k'}}' C_{k'}^{(1)}(t)\,|k'\rangle, \tag{12}$$

where the primed summation has excluded the case $k' = k_{\eta R}$. Substitution of Eq. (12) into Eq. (11) gives

$$\frac{dC_{k'}^{(1)}}{dt} = -\frac{i}{\hbar}\cos(\Omega t)\, e^{\zeta t}\, e^{i\omega_{K'K}^\eta t}\,\langle k'|F_{K'K}^\eta(x)|k_{\eta R}\rangle. \tag{13}$$

Here, $K' = k' + m\alpha_0\overline{\eta}/\hbar$,

$$\omega_{K'K}^\eta = \hbar(K'^2 - K^2)/(2m), \tag{14}$$

and

$$F_{K'K}^\eta(x) = \frac{\alpha_1\overline{\eta}\hbar}{2}\left(K' + K - \frac{2m\alpha_0\overline{\eta}}{\hbar}\right) f(x) + U_1\, g(x). \tag{15}$$

It is noted that α_0 appears in Eq. (15) through the wave vectors $k_{\eta R}$ and k', whereas the corresponding wave vectors K and K', respectively, directly associate to their group velocities and energies, in the conventional way. Integrating Eq. (13) gives

$$C_{k'}^{(1)}(t) = -\frac{F_{K'K}^\eta}{2\hbar}\left[\frac{e^{i(\omega_{K'K}^\eta + \Omega - i\zeta)t}}{\omega_{K'K}^\eta + \Omega - i\zeta} + \frac{e^{i(\omega_{K'K}^\eta - \Omega - i\zeta)t}}{\omega_{K'K}^\eta - \Omega - i\zeta}\right] \tag{16}$$

for $k' \neq k_{\eta R}$ and $F_{K'K}^\eta = \langle K'|F_{K'K}^\eta(x)|K\rangle$.

We substitute Eq. (16) into Eq. (12) to obtain $\psi_\eta^{(1)}(x,t)$. More importantly, our interest is to extract from the integral form of $\psi_\eta^{(1)}(x,t)$ the reflection coefficients $r_{\eta n}$ for $n = \pm 1$. On the left-hand side of the finger-gate capacitor, and far from the gate-induced fields, we impose the expected form

$$\psi_\eta^{(1)}(x,t) = \sum_{n=\pm 1} r_{\eta n}\, e^{ik_{\eta L}^n x}, \tag{17}$$

where $k^n_{\eta L} = -K_n - m\alpha_0\overline{\eta}/\hbar$ is the wave vector for left-going state at energy $\mu_n = \mu + n\hbar\Omega = \hbar^2 K_n^2/(2m)$. In short, $\psi^{(1)}_\eta(x,t)$ in Eq. (17) is for the reflection waves. The fact that the reflection waves do not depend on t, even though $C^{(1)}_{k'}(t)$ does, should not cause any alarm. It is because the appropriate time dependencies will be recovered in the Schrödinger picture, and are in accordance to the sideband-process picture.

Conversion of $\psi^{(1)}_\eta(x,t)$ in Eq. (12) into the form given by Eq. (17) is facilitated by writing in $C^{(1)}_{k'}(t)$ the factor $F^\eta_{K'K}$ in its integral form, and keeping x to locate on the left-hand side of all locations involved in the spatial integral. The reflection waves expression is given by

$$\psi^{(1)}_\eta = -\sum_{n=\pm1} \frac{e^{-i\frac{m\alpha_0}{\hbar}\overline{\eta}x}}{4\pi\hbar} \int_{-\infty}^{\infty} dx'\, e^{iKx'} \int_{-\infty}^{\infty} dK' \times F^\eta_{K'K}(x')\, \frac{e^{-iK'|x-x'|}\; e^{i(\omega_{K'K}-n\Omega)t}}{\omega_{K'K} - n\Omega - i\zeta}, \tag{18}$$

where superscript η is dropped from $\omega_{K'K}$ when K' becomes the integration variable, and the relevant range of x' is determined by the field's range even though the integration is over the formal full range of x'.

Performing the K' integral gives

$$\psi^{(1)}_\eta = -\sum_{n=\pm1} \frac{mi}{2\hbar^2}\, e^{-i\frac{m\alpha_0}{\hbar}\overline{\eta}x} \int_{-\infty}^{\infty} dx'\, e^{iKx'} \times \frac{e^{iK_n|x-x'|}}{K_n}\, F^\eta_{-K_n,K}(x'), \tag{19}$$

where $K_{\pm1} = \sqrt{K^2 \pm 2m\Omega/\hbar}$. For the case when K_- becomes imaginary, the convention $K_- = i\sqrt{2m\Omega/\hbar - K^2}$ is used. It is straightforward to see that Eq. (19) is of the form in Eq. (17). The reflection coefficients are then obtained to give

$$r_{\eta n} = -\frac{mi}{2\hbar^2 K_n} \int_{-\infty}^{\infty} dx'\, F^\eta_{-K_n,K}(x')\, e^{i(K+K_n)x'}. \tag{20}$$

Substituting Eq. (15) into Eq. (20) gives

$$r_{\eta n} = \frac{im\overline{\eta}}{4\hbar}\left[\alpha_1\left(1 - \frac{K}{K_n} + \frac{2m\alpha_0}{\hbar K_n}\overline{\eta}\right)\mathcal{F}_{nK} - \frac{2U_1\overline{\eta}}{\hbar K_n}\mathcal{G}_{nK}\right], \tag{21}$$

where

$$\mathcal{F}_{nK} = \int_{-\infty}^{\infty} dx'\, f(x')\, e^{i(K+K_n)x'}, \qquad \mathcal{G}_{nK} = \int_{-\infty}^{\infty} dx'\, g(x')\, e^{i(K+K_n)x'} \tag{22}$$

are the integrals involving the spatial profiles of, respectively, the ac SOI and potential energy fields. Terms inside the square brackets of Eq. (21) that contain the $\overline{\eta}$ factor contribute to genuine spin-dependent transmissions. In addition, terms inside the parentheses contain the breaking of spin symmetry by α_0 during reflection in the sideband processes. This is due to the anticommutator in Eq. (9), which will be proportional to the sum of the incident wave vector $(K - m\alpha_0\overline{\eta}/\hbar)$ and the reflection wave vector $(-K_n - m\alpha_0\overline{\eta}/\hbar)$ in a n-sideband process. The magnitude of the wave-vector sum, given by $(K - K_n) - 2m\alpha_0\overline{\eta}/\hbar$, becomes spin dependent as long as $n \neq 0$. Moreover, that the resonant sideband nature weighs more on $n = -1$ process guarantees its breaking of the spin symmetry by a nonzero α_0.

The total dc spin-dependent transmission T^η_{RL}, from the left to right electrodes, is given by $T^\eta_{RL} = {\sum_n}' T^\eta_{RL}(n)$. Here, $T^\eta_{RL}(n) = |t_{\eta n}|^2\sqrt{\frac{\mu_n}{\mu}}$, the primed summation sums over n where $\mu_n \geqslant 0$, and the factor $\sqrt{\mu_n/\mu}$ is the group velocity ratio [40,43]. The calculation of T^η_{RL} is more easily done than its direct calculation, through using the current conservation relation

$$T^\eta_{RL} + R^\eta_{RL} = 1, \tag{23}$$

where $R^\eta_{RL} = {\sum_n}' |r_{\eta n}|^2\sqrt{\frac{\mu_n}{\mu}}$.

Furthermore, our interest is on the difference in the total spin-dependent transmission $T^\uparrow_{RL} - T^\downarrow_{RL}$. For presentation sake, we have replaced $\eta = 1$ (-1) by $\eta = \uparrow(\downarrow)$. Substituting the first-order $r_{\eta n}$ expressions (21) into Eq. (23), we obtain, after some algebra, the lowest- (second-) order results for the dc spin-dependent transmission difference, as is presented below:

$$\Delta T^{\rm s}_{RL} = T^\uparrow_{RL} - T^\downarrow_{RL} = {\sum_{n=\pm1}}' \frac{1}{2}\left(\frac{m}{\hbar}\right)^2 \frac{m\alpha_1}{\hbar K}\left(1 - \frac{K}{K_n}\right) \times\left[\alpha_0\alpha_1|\mathcal{F}_{nK}|^2 - \frac{U_1}{m}{\rm Re}(\mathcal{F}^*_{nK}\mathcal{G}_{nK})\right]. \tag{24}$$

Equation (24) is our key result. First of all, it shows that $\Delta T^{\rm s}_{RL}$ is nonzero. It remains nonzero even when $\alpha_0 = 0$. The K^{-1} factor in $m\alpha_1/(\hbar K)$ comes from the incident density of states, and in $(1 - K/K_n)$ the factor K_n^{-1} is reckoned to represent the corresponding density of states for the $n = \pm1$ sidebands.

In a spin-pumping situation, when incident states come from both electrodes, the total charge current, which is related to $(T^\uparrow_{RL} + T^\downarrow_{RL}) - (T^\uparrow_{LR} + T^\downarrow_{LR})$, is zero. This is because of the time-reversal-symmetry result, given by

$$T^\pm_{RL} = T^\mp_{LR}. \tag{25}$$

On the other hand, the total spin current, which is related to $(T^\uparrow_{RL} - T^\downarrow_{RL}) - (T^\uparrow_{LR} - T^\downarrow_{LR})$, becomes related to $2\Delta T^{\rm s}_{RL}$.

Two mechanisms that contribute to $\Delta T^{\rm s}_{RL}$ are shown in Eq. (24). The term that involves α_1 and U_1 corresponds to the simultaneous coupling of the ac SOI and potential energy fields with the electrons. The term that involves α_1 and α_0 corresponds to the simultaneous coupling of the static SOI and ac SOI fields with the electrons.

Resonant nature of the mechanisms is shown also in Eq. (24). It is through the factor K_n^{-1}, or the corresponding sideband density of states, for $n = -1$. When $K_{-1} \to 0^+$ (or $\mu - \hbar\Omega \to 0^+$), the $n = -1$ sideband process will hit the subband bottom. Contribution from this sideband process is large due to the singular density of states. In the vicinity of this resonant sideband regime, high-order processes are important and a full sideband numerical treatment is provided by our time-dependent scattering matrix method (Sec. II). It is worth

pointing out that our numerical results are found (not shown) to match those given by Eq. (24) in small-U_1 cases.

The induced-field profiles entering Eq. (24) through $\mathcal{F}_{nK}$ and $\mathcal{G}_{nK}$, in Eq. (22), show that our nonzero $\Delta T^{\rm s}_{RL}$ finding should hold regardless of the profiles. The induced-field profiles could only affect our finding quantitatively and not qualitatively. We drive this finding home by showing, in the following, that Eq. (24) has covered the perturbation results in [21] as a special case. Setting $U_1 = 0$ while keeping nonzero α_1, which can be achieved for a symmetric finger-gate capacitor ($z_A = |z_B|$), and choosing $f(x) = \Theta(L/2 - |x|)$ and α_0 finite, we get from Eq. (20)

$$r^{\rm a}_{\eta n} = \frac{\alpha_1 m n \overline{\eta} i}{2\hbar K_n} \sin\left[(K + K_n)\frac{L}{2}\right]\left[n + \frac{\hbar k_{\eta R}}{m\Omega}(K - K_n)\right]. \tag{26}$$

Here, $n = \pm 1$, $\Theta(x)$ is a step function, and superscript "a" denotes the case for a steplike profile for the ac SOI. The expression in Eq. (26) equals that in [21]. The essential spin dependence in $r^{\rm a}_{\eta n}$ enters through $k_{\eta R}$ in Eq. (26).

III. SCATTERING MATRIX METHOD

The time-dependent scattering matrix method is to discretize the induced-field region into small slices of ac potentials, each has a width Δ along x. The reflection and transmission coefficients of each such slice is then calculated. The scattering properties of neighboring pieces will be convoluted to obtain the scattering matrix of a finite width of such an ac potential. This convolution procedure will stop when the entire range of the induced fields is covered. The scattering matrix method aims to provide a decent numerical scheme for the handling of the evanescent waves. The present method has included the SOI to an earlier work, in Ref. [39], of one of the author.

The Hamiltonian describing an ac potential slice, located within $|x - x_j| \leqslant \Delta/2$, is taken from Eq. (9) except that a slicelike envelope $\Theta(\Delta/2 - |x - x_j|)$ is imposed upon the field profile functions $f(x)$ and $g(x)$, to give

$$H'_{\eta j} = H^0_\eta + U_1 \cos(\Omega t) g(x)\,\Theta(\Delta/2 - |x - x_j|) + \frac{\alpha_1 \overline{\eta}}{2}\cos(\Omega t)\{f(x)\,\Theta(\Delta/2 - |x - x_j|), p_x\}. \tag{27}$$

We further approximate $g(x)$ by $g(x_j)$ and $f(x)$ by $f(x_j)$ after the evaluation of the anticommutator. Consider a right-going state $|k^{n_{\rm i}}_{\eta R}\rangle$ incident upon the slice potential $(H'_{\eta j} - H^0_\eta)$ in Eq. (27), the total scattering state, represented by reflection coefficients $r_{\eta j}(n,n_{\rm i})$ and transmission coefficients $t_{\eta j}(n,n_{\rm i})$, are given by the form

$$\psi_{\eta j}(x,t) = \begin{cases} \sum_n \left[e^{ik^{n_{\rm i}}_{\eta R}x}\delta_{nn_{\rm i}} + r_{\eta j}(n,n_{\rm i})e^{ik^n_{\eta L}x}\right]e^{-i\mu_n t/\hbar} & \text{for } x < x_{j-}, \\ e^{-\frac{i\sin(\Omega t)}{\hbar\Omega}[(\frac{\alpha_1\overline{\eta}}{2})[2f(x_j)p_x + \frac{\hbar}{i}f'(x_j)] + U_1 g(x_j)]} \sum_{n'}\left[A_{\eta j}(n',n_{\rm i})e^{ik^{n'}_{\eta R}x} + B_{\eta j}(n',n_{\rm i})e^{ik^{n'}_{\eta L}x}\right]e^{-i\mu_{n'}t/\hbar} & \text{for } |x - x_j| < \frac{\Delta}{2}, \\ \sum_n \left[t_{\eta j}(n,n_{\rm i})e^{ik^n_{\eta R}x}\right]e^{-i\mu_n t/\hbar} & \text{for } x > x_{j+}, \end{cases} \tag{28}$$

where $x_{j\pm} = x_j \pm \Delta$. The wave-function form in the $|x - x_j| < \frac{\Delta}{2}$ region of Eq. (28) can be shown, by direct substitution, to satisfy the time-dependent Schrödinger equation for the Hamiltonian in Eq. (27). The slicelike envelope in the anticommutator contributes to the wave-function matching conditions, given by

$$\left.\frac{\partial\psi_{\eta j}}{\partial x}\right|_{x_{j\pm}-0^+}^{x_{j\pm}+0^+} \pm \frac{m\alpha_1\overline{\eta}}{i\hbar}\cos(\Omega t)\, f(x)\,\psi_{\eta j}\Big|_{x_{j\pm}} = 0. \tag{29}$$

By invoking the relation $e^{iz\sin(\Omega t)} = \sum_n J_n(-z)e^{-in\Omega t}$, we separate different time dependencies to obtain, after some algebra, the equations for coefficients $A_{\eta j}(n,n_{\rm i})$ and $B_{\eta j}(n,n_{\rm i})$ inside the potential slice. Here, $J_n(z)$ is Bessel function of the first kind. The equations for the coefficients are given by

$$\begin{bmatrix} \mathbf{M}_{11} & \mathbf{M}_{12} \\ \mathbf{M}_{21} & \mathbf{M}_{22} \end{bmatrix}\begin{bmatrix} \mathbf{A}_{\eta j}(n_{\rm i}) \\ \mathbf{B}_{\eta j}(n_{\rm i}) \end{bmatrix} = \begin{bmatrix} \mathbf{C}_{\eta j}(n_{\rm i}) \\ 0 \end{bmatrix}. \tag{30}$$

Here, $\mathbf{A}_{\eta j}(n_{\rm i})$, $\mathbf{B}_{\eta j}(n_{\rm i})$, and $\mathbf{C}_{\eta j}(n_{\rm i})$ are column vectors of $(2N_{\rm SB}+1)\times 1$ dimensions, and $2N_{\rm SB}+1$ is the number of sidebands used. Typically, in this work, we have $N_{\rm SB} \sim 30$. At $x = x_{j-}$, the matrices and their matrix elements are

$$(\mathbf{M}_{11})_{nn'} = (-1)^{n-n'}J_{n-n'}\left(Z^{n'}_{jR}\right)e^{ik^{n'}_{\eta R}x_{j-}} \times\left[k^n_{\eta L} - k^{n'}_{\eta R} - \frac{m\alpha_1\eta(n-n')}{\hbar\, Z^{n'}_{jR}}f(x_{j-})\right],$$
$$\left(\mathbf{M}_{12}\right)_{nn'} = (-1)^{n-n'}J_{n-n'}\left(Z^{n'}_{jL}\right)e^{ik^{n'}_{\eta L}x_{j-}} \times\left[k^n_{\eta L} - k^{n'}_{\eta L} - \frac{m\alpha_1\eta(n-n')}{\hbar\, Z^{n'}_{jL}}f(x_{j-})\right]. \tag{31}$$

At $x = x_{x_{j+}}$, the matrix elements are

$$(\mathbf{M}_{21})_{nn'} = (-1)^{n-n'}J_{n-n'}\left(Z^{n'}_{jR}\right)e^{ik^{n'}_{\eta R}x_{j+}} \times\left[k^n_{\eta R} - k^{n'}_{\eta R} - \frac{m\alpha_1\eta(n-n')}{\hbar\, Z^{n'}_{jR}}f(x_{j+})\right], \tag{32}$$
$$(\mathbf{M}_{22})_{nn'} = (-1)^{n-n'}J_{n-n'}(Z^{n'}_{jL})\,e^{ik^{n'}_{\eta L}x_{j+}} \times\left[k^n_{\eta R} - k^{n'}_{\eta L} - \frac{m\alpha_1\eta(n-n')}{\hbar\, Z^{n'}_{jL}}f(x_{j+})\right]. \tag{33}$$

The column vector $(\mathbf{C}_{\eta j})_n = \delta_{nn_{\rm i}}[k^n_{\eta L} - k^n_{\eta R}]e^{ik^n_{\eta R}x_{j-}}$ and $Z^n_{jR} = \frac{1}{\hbar\Omega}[\alpha_1\eta f(x_j)\hbar k^n_{\eta R} + \frac{\alpha_1\eta\hbar}{2i}f'(x_j) - U_1 g(x_j)]$.

Solving Eq. (30) for $\mathbf{A}_{\eta j}(n_{\rm i})$ and $\mathbf{B}_{\eta j}(n_{\rm i})$, the reflection and transmission coefficients can then be calculated from the following equations:

$$r_{\eta j}(n,n_{\rm i}) = \sum_{n'}(-1)^{n-n'}\left[J_{n-n'}\left(Z^{n'}_{jR}\right)e^{i(k^{n'}_{\eta R}-k^{n}_{\eta mL})x_{j-}}\,A_{\eta j}(n',n_{\rm i}) + J_{n-n'}\left(Z^{n'}_{jL}\right)e^{i(k^{n'}_{\eta L}-k^{n}_{\eta L})x_{j-}}\,B_{\eta j}(n',n_{\rm i})\right] - \delta_{nn_{\rm i}}\,e^{i(k^{n}_{\eta R}-k^{n}_{\eta L})x_{j-}} \tag{34}$$

and

$$t_{\eta j}(n,n_{\rm i}) = \sum_{n'}(-1)^{n-n'}\left[J_{n-n'}\left(Z^{n'}_{jR}\right)e^{i(k^{n'}_{\eta R}-k^{n}_{\eta R})x_{j+}}\,A_{\eta j}(n',n_{\rm i}) + J_{n-n'}\left(Z^{n'}_{jL}\right)e^{i(k^{n'}_{\eta L}-k^{n}_{\eta R})x_{j+}}\,B_{\eta j}(n',n_{\rm i})\right].$$

We consider also left-going incident state $|k^{n_{\rm i}}_{\eta L}\rangle$ and obtain the reflection $\tilde{r}_{\eta j}(n,n_{\rm i})$ and transmission $\tilde{t}_{\eta j}(n,n_{\rm i})$ coefficients with the same procedure above. All these coefficients are used in our transmission calculation through the entire ac induced fields with smooth spatial profiles.

In the total transmission calculation, the total waves between the jth and $(j+1)$th potential slices are denoted by coefficients $a_{\eta j}(n)$ and $b_{\eta j}(n)$ for, respectively, right- and left-going waves in the nth sideband. The scattering matrix $\mathbf{S}_\eta(j-1,j)$, of dimensions $(4N_{\rm SB}+2)\times(4N_{\rm SB}+2)$, connecting the waves on the two sides of the jth potential slice is given by

$$\mathbf{S}_\eta(j-1,j) = \begin{bmatrix} \mathbf{t}_{\eta j} & \tilde{\mathbf{r}}_{\eta j} \\ \mathbf{r}_{\eta j} & \tilde{\mathbf{t}}_{\eta j} \end{bmatrix}, \tag{35}$$

where

$$\begin{bmatrix} \mathbf{a}_{\eta j} \\ \mathbf{b}_{\eta,j-1} \end{bmatrix} = \mathbf{S}_\eta(j-1,j)\begin{bmatrix} \mathbf{a}_{\eta,j-1} \\ \mathbf{b}_{\eta j} \end{bmatrix}. \tag{36}$$

For the convolution of the scattering matrices to obtain $\mathbf{S}_\eta(0,N)$, when N is the total number of potential slices, we need to use an inverse transfer matrix $\mathbf{I}_\eta(j)$, given by

$$\mathbf{I}_\eta(j) = \begin{bmatrix} \mathbf{t}^{-1}_{\eta j} & -\mathbf{t}^{-1}_{\eta j}\,\tilde{\mathbf{r}}_{\eta j} \\ \mathbf{r}_{\eta j}\,\mathbf{t}^{-1}_{\eta j} & \tilde{\mathbf{t}}_{\eta j} - \mathbf{r}_{\eta j}\mathbf{t}^{-1}_{\eta j}\,\tilde{\mathbf{r}}_{\eta j} \end{bmatrix}, \tag{37}$$

where

$$\begin{bmatrix} \mathbf{a}_{\eta,j-1} \\ \mathbf{b}_{\eta,j-1} \end{bmatrix} = \mathbf{I}_\eta(j)\begin{bmatrix} \mathbf{a}_{\eta j} \\ \mathbf{b}_{\eta j} \end{bmatrix}. \tag{38}$$

Finally, the scattering matrix $\mathbf{S}_\eta(0,j)$ can be expressed in terms of $I_\eta(j)$ and $\mathbf{S}_\eta(0,j-1)$ [39], given by

$$\begin{aligned}
\mathbf{S}_\eta(0,j)_{11} &= [\mathbf{I}_\eta(j)_{11} - \mathbf{S}_\eta(0,j-1)_{12}\,\mathbf{I}_\eta(j)_{21}]^{-1} \\
&\quad\times \mathbf{S}_\eta(0,j-1)_{11}, \\
\mathbf{S}_\eta(0,j)_{12} &= [\mathbf{I}_\eta(j)_{11} - \mathbf{S}_\eta(0,j-1)_{12}\,\mathbf{I}_\eta(j)_{21}]^{-1} \\
&\quad\times [\mathbf{S}_\eta(0,j-1)_{12}\,\mathbf{I}_\eta(j)_{22} - \mathbf{I}_\eta(j)_{12}], \\
\mathbf{S}_\eta(0,j)_{21} &= \mathbf{S}_\eta(0,j-1)_{21} \\
&\quad+ \mathbf{S}_\eta(0,j-1)_{22}\mathbf{I}_\eta(j)_{21}\mathbf{S}_\eta(0,j)_{11}, \\
\mathbf{S}_\eta(0,j)_{22} &= \mathbf{S}_\eta(0,j-1)_{22}\mathbf{I}_\eta(j)_{22} \\
&\quad+ \mathbf{S}_\eta(0,j-1)_{22}\mathbf{I}_\eta(j)_{21}\mathbf{S}_\eta(0,j)_{12}.
\end{aligned} \tag{39}$$

Iterating Eq. (39) leads us eventually to $\mathbf{S}_\eta(0,N)$.

Now, for the case of right-going state $|k_{\eta R}\rangle$ incident upon the smooth-profiled ac induced fields $\mathbf{b}_{\eta N}=0$ and $a_{\eta 0}(n)=\delta_{n0}$. Then, the transmission and reflection coefficients are given, respectively, by $\mathbf{t}_\eta = \mathbf{S}_\eta(0,N)_{11}\,\mathbf{a}_{\eta 0}$ and $\mathbf{r}_\eta = \mathbf{S}_\eta(0,N)_{21}\,\mathbf{a}_{\eta 0}$. On the same token, we have $\tilde{\mathbf{t}}_\eta = \mathbf{S}_\eta(0,N)_{12}\,\mathbf{b}_{\eta N}$ and $\tilde{\mathbf{r}}_\eta = \mathbf{S}_\eta(0,N)_{22}\,\mathbf{b}_{\eta N}$ for the left-going incident case. Here, $b_{\eta N}(n) = \delta_{n0}$ and $\mathbf{a}_{\eta 0}=0$.

The net spin current $I^{\rm s}_{RL}$, in units of $\hbar/2$, due to right-going incident carriers is given by

$$I^{\rm s}_{RL} = \sum_\eta \frac{\eta}{h}\int_0^\mu T^\eta_{RL}(E)\,dE, \tag{40}$$

and the net pumped spin current

$$I^{\rm s}_{\rm p} = I^{\rm s}_{RL} - I^{\rm s}_{LR} = 2I^{\rm s}_{RL}. \tag{41}$$

Subsequently, the net pumped spin per cycle $N^{\rm s}_{\rm p} = \frac{2\pi}{\Omega}\,I^{\rm s}_{\rm p}$.

IV. NUMERICAL RESULTS AND DISCUSSIONS

In this section, we present numerical results for the spin-pumping characteristics in a quantum channel due to a single finger-gate capacitor (FGC). Modulated by ac biases, the FGC induces both ac potential and SOI in the quantum channel, which has no static SOI ($\alpha_0=0$). The general spin-pumping characteristics of our interest are exhibited in their dependence on both μ and Ω.

Material parameters for the numerical calculations are the same as for InSb, with effective mass $m = 0.0139\,m_{\rm e}$ and SOI coupling constant $\hbar\lambda = 5.23\ {\rm e}\cdot{\rm nm}^2$ [13]. Here, $m_{\rm e}$ and e are, respectively, the electron mass and charge (magnitude). We define physical quantity units out of typical electron density $n_{\rm e} = 10^{12}\ {\rm cm}^{-2}$, with wave vector unit $k^* = \sqrt{2\pi n_{\rm e}} = 2.5\times 10^8\ {\rm m}^{-1}$, length unit $l^* = 1/k^* = 4$ nm, and frequency unit $f^* = E^*/h = 41$ THz, where $E^* = \hbar^2 k^{*2}/(2m) = 171$ meV.

For the numerical examples below, the FGC parameters are chosen to be $L = 12\,l^*$, $z_A = 6\,l^*$, and $z_B = -3\,l^*$. The ac bias parameters, in Eq. (6), are chosen to be $V_1 = 0.15$ V for the bias amplitude, and Ω ranges between $0.01\Omega^* \sim 0.03\,\Omega^*$ for the bias angular frequency. Here, $\Omega^* = 2\pi f^*$.

Presented in Fig. 2 is $\Delta T^{\rm s}_{RL}$ and its μ and Ω characteristics. The most important result is that the $\Delta T^{\rm s}_{RL}$ are quite significant in their values. For instance, peak values $\Delta T^{\rm s}_{RL} \approx 0.12$, near $\mu = 0.0065$ for $\Omega = 0.013$, and $\Delta T^{\rm s}_{RL} \approx -0.08$, near $\mu = 0.055$ for $\Omega = 0.02$. Equally important is that for the patches of positive, or negative, $\Delta T^{\rm s}_{RL}$ in the μ-Ω plane, the positive $\Delta T^{\rm s}_{RL}$ patches appear to dominate over their counterparts in both their $\Delta T^{\rm s}_{RL}$ magnitudes and their areal sizes. This is crucial for the net spin pumping, as will be presented in Fig. 3. The patches of positive, or negative, $\Delta T^{\rm s}_{RL}$ also exhibit two other features. First, smaller-sized (larger-sized) patches occur in the smaller (larger) Ω region. On the one hand, the resonant sideband processes introduce a natural energy scale $\hbar\Omega$, which tends to bring forth smaller μ structures in the smaller Ω region. We indicate, as a guide, the sideband-process

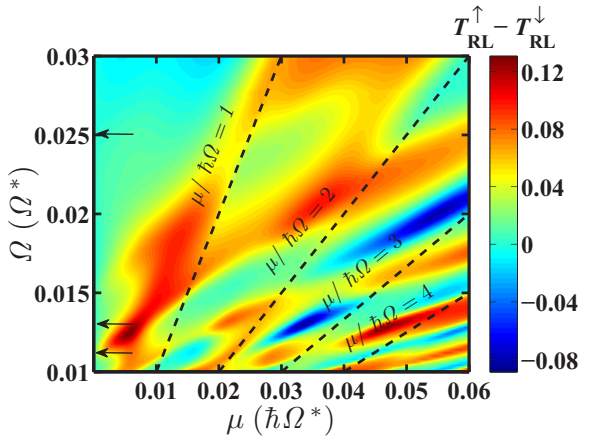

FIG. 2. Colored contours for $T_{RL}^{\uparrow} - T_{RL}^{\downarrow}$ as a function of incident energy μ and pumping frequency Ω. The finger-gate parameters are $L = 12l^*$, $z_A = 6l^*$, $z_B = -3l^*$, with $l^* = 4$ nm, and pumping bias amplitude $V_1 = 0.15$ V. Indicated by dashed lines are cases for $\mu = n\hbar\Omega$. Frequencies depicted by black arrows are selected for further analysis in Figs. 4– 6.

conditions $\mu = n\hbar\Omega$ by black dashed lines. On the other hand, as is shown in Figs. 4 and 5, smaller (larger) Ω has a larger (smaller) sideband effect which, in turn, causes modifications to the patch structures. Second, ΔT_{RL}^{s} shows nonmonotonic variations in either increasing μ, for a given Ω, or increasing Ω, for a given μ. We will look into the nonmonotonic variation along μ in Fig. 5 for three Ω values depicted by black arrows in Fig. 2. The nonmonotonic variation along the vicinity of $\mu = \Omega$ will be shown in Fig. 6.

The net spin pumped per cycle N_p^s and its characteristics in the μ-Ω plane are presented in Fig. 3. This is a direct integration of Fig. 2, over energy and up to μ, for a given Ω, as is given by Eqs. (40) and (41). That $N_p^s > 0$ in the entire μ-Ω plane, shown in Fig. 3, reflects the dominance of the positive ΔT_{RL}^{s} patches over its counterparts in Fig. 2. The optimal N_p^s does not necessarily occur at where ΔT_{RL}^{s} is peaked, such as at

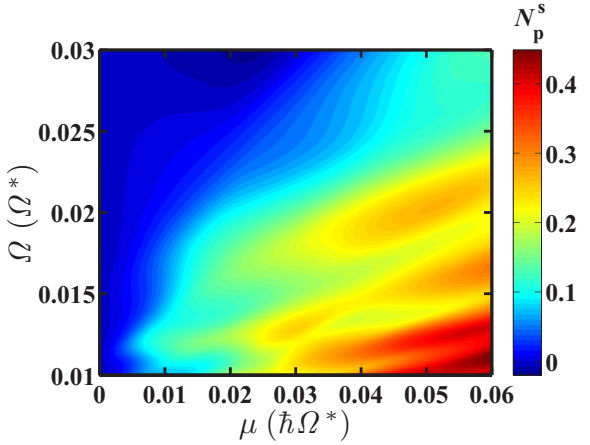

FIG. 3. Colored contours for net spin N_p^s pumped per cycle as a function of μ and Ω. Positive N_p^s corresponds to N_p^s net spin-up (along $\hat{y}$) electrons being pumped from left to right electrodes. Pumping bias amplitude $V_1 = 0.15$ V. Finger-gate parameters are the same as in Fig. 2.

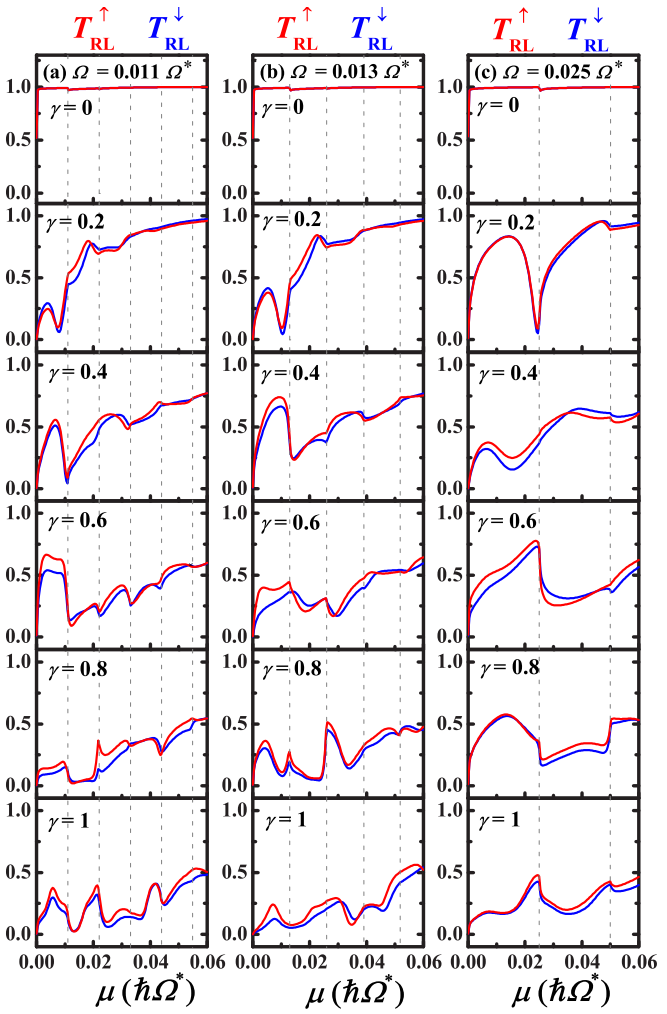

FIG. 4. μ characteristics of T_{RL}^{η}, the right-going spin-dependent transmission, for some ac potential field strength γU_1. Pumping frequencies fixed at (a) $\Omega = 0.011\,\Omega^*$, (b) $\Omega = 0.013\,\Omega^*$, and (c) $\Omega = 0.025\,\Omega^*$ are indicated in Fig. 2 by arrows. The finger-gate and pumping parameters are as in Fig. 2 except that the ac potential field strength has $\gamma = 0$, 0.2, 0.4, 0.6, 0.8, and 1.0. Vertical dashed lines indicate $\mu = n\hbar\Omega$.

$\Omega = 0.013$. Rather, whether ΔT_{RL}^{s} could manage to maintain the same sign over a large-μ region is another important factor. It turns out that the optimal spin pumping occurs at $\Omega = 0.011$, or $f = 0.45$ THz, for $\mu = 0.06$. The optimal pumped spin per cycle is $N_p^s = 0.45$. This would be equivalent to an electric current of $N_p^s ef = 32$ nA, had each pumped spin been given a charge e. The spin-pumping effect is thus significant.

Resonant sideband origin for the spin pumping shown in Fig. 2 is identified through our analysis in Figs. 4 and 5. The μ characteristics of T_{RL}^{η} and ΔT_{RL}^{s} are presented for various values of the ac potential field strength γU_1 in, respectively, Figs. 4 and 5. For analysis purposes, the parameter γ is introduced artificially to help tune only the coupling strength of the ac potential U_1 while keeping that of the ac SOI α_1 constant. Cases for $\gamma = 1$ correspond to those shown in Fig. 2. Presented in Fig. 4 (Fig. 5) is T_{RL}^{η} (ΔT_{RL}^{s}) in incremental order of γ between [0, 1]. For the clarity of presentation, a relative upward shift of 0.3 between curves of consecutive γ is

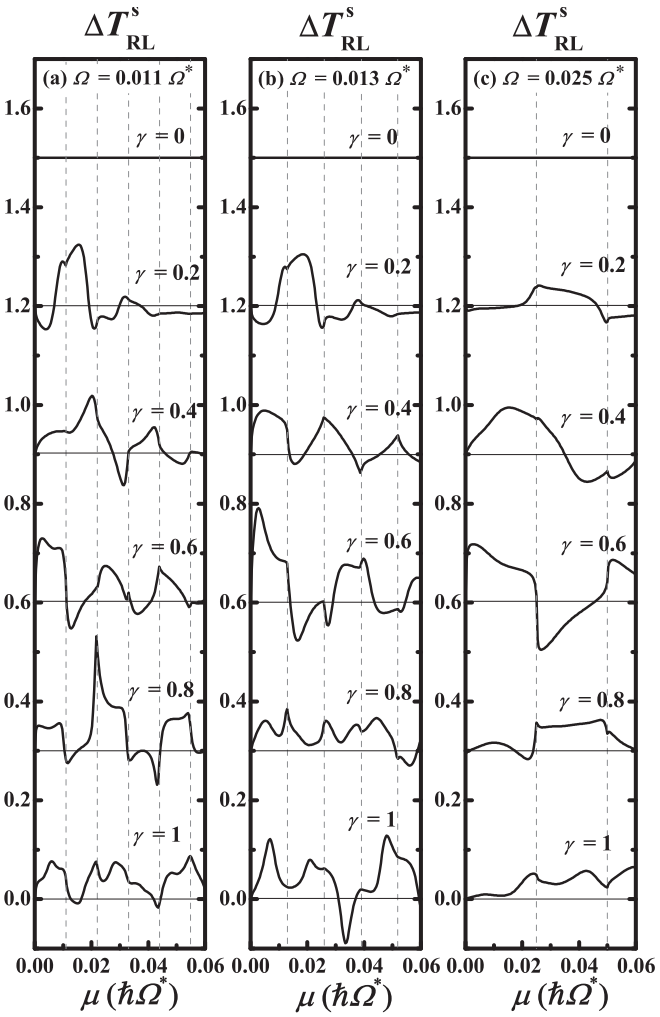

FIG. 5. μ characteristics of $\Delta T^{s}_{RL} = T^{\uparrow}_{RL} - T^{\downarrow}_{RL}$ for some ac potential field strength γU_1. Pumping frequencies are fixed at (a) $\Omega = 0.011\,\Omega^*$, (b) $\Omega = 0.013\,\Omega^*$, and (c) $\Omega = 0.025\,\Omega^*$ (indicated in Fig. 2). The finger-gate and pumping parameters are as in Fig. 2 except that the ac potential field strength has $\gamma = 0$, 0.2, 0.4, 0.6, 0.8, and 1.0. Vertical dashed lines indicate $\mu = n\hbar\Omega$.

adopted in Fig. 5. Selected pumping frequencies Ω, indicated in Fig. 2 and presented in Figs. 4 and 5, are of values (a) 0.011, (b) 0.013, and (c) 0.025.

Typical resonant sideband features, the dip structures in T^{η}_{RL} at $\mu = \hbar\Omega$, are shown in Fig. 4 for $\gamma = 0$ and $\gamma = 0.2$ cases. It is associated with the temporal trapping, or the forming of a quasibound state just beneath the subband bottom, of the electron in the vicinity of the ac field [40]. The dip structures are small for the $\gamma = 0$ case, showing weak time-modulation effects of the ac SOI, and $T^{\uparrow}_{RL} = T^{\downarrow}_{RL}$ shows that there is no spin pumping, as is expected according to Eq. (24) when $\alpha_0 = 0$. Deeper and broader dip structures for the $\gamma = 0.2$ case show an increase in the time-modulation effects. Of the three frequencies (for $\gamma = 0.2$) shown, the dip structures in Fig. 4(c) ($\Omega = 0.025\Omega^*$) bear the resonant characteristics closest to typical low sideband processes [21], namely, with the dip occurring at $\mu = \hbar\Omega$ while T^{η}_{RL} recovers to high values, less than but close to unity, on both sides of the $\mu = \hbar\Omega$

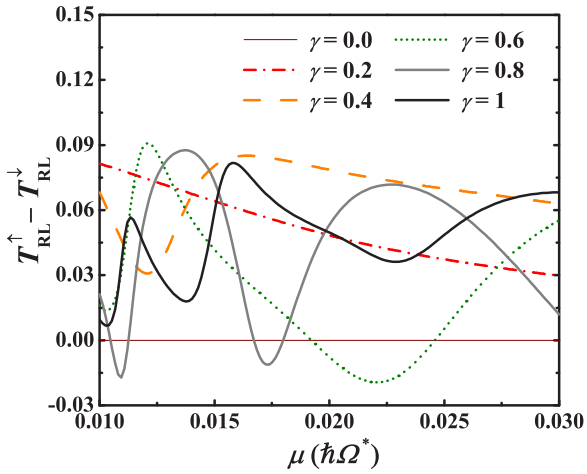

FIG. 6. μ characteristics of $T^{\uparrow}_{RL} - T^{\downarrow}_{RL}$ along $\hbar\Omega = \mu^+$ for fixed ac potential field strength γU_1. The finger-gate and pumping parameters are as in Fig. 2 except that the ac potential field strength has $\gamma = 0$, 0.2, 0.4, 0.6, 0.8, and 1 denoted by, respectively, the brown (thin solid), red (dotted-dashed), orange (dashed), green (dotted), gray (medium solid), and black (thick solid) curves. $\mu^+ = \mu + 10^{-6}$.

position. As Ω decreases, from $\Omega = 0.013\Omega^*$ in Fig. 4(b) to $\Omega = 0.011\Omega^*$ in Fig. 4(a), the progressively lowering in T^{η}_{RL} in the $\mu < \hbar\Omega$ region shows that more sideband processes are involved in the establishment of the resonance. This more sideband-processes interpretation is further confirmed by the fact that the dip structures are more leftward shifted in Fig. 4(a) than in 4(b) away from the $\mu = \hbar\Omega$ position for $\gamma = 0.2$. This is corroborated with the lowering of the quasibound state by the increasing in the time-modulation field strengths [40]. That lower frequency tends to bring forth more sideband processes is also consistent with the Ω^{-1} dependence in the dimensionless strengths Z^{n}_{jR} and Z^{n}_{jL} in Eq. (31). For higher γ values in Fig. 4, even more sideband processes come into play, the resonant sideband features thus evolve from simple dip structures to diplike or peaklike or kinklike structures at $\mu = n\hbar\Omega$. In our numerical calculation, we have included up to $2N_{SB} + 1$ sidebands, for $N_{SB} = 30$.

The ΔT^{s}_{RL} curves obtained from Fig. 4 are presented in Fig. 5. Two key features are observed. The energy structures in ΔT^{s}_{RL} are essentially given by $\hbar\Omega$, which is a manifestation of the resonant sideband features, the $\mu = n\hbar\Omega$ structures we obtained in Fig. 4. As γ increases toward unity, the negative ΔT^{s}_{RL} regions are either being suppressed to much smaller magnitudes, such as the trend shown in Fig. 5(a), or being pushed towards larger μ, such as the trend shown in Figs. 5(b) or 5(c). Both trends are important for spin pumping. Thus, we have established that resonant sideband processes contribute significantly to the spin pumping. On the other hand, one should be cautioned that too large an ac potential field might not be a favorable choice for spin pumping. Towards this end, we consider the case of a single-finger gate, when the z_B gate of the single-gate capacitor is removed. The ac potential field in the QC is increased while the ac SOI is decreased. Indeed, our calculation shows that N^{s}_{p}, though remaining within a reasonable range, is much reduced. Specifically, for a pumping

frequency of $\Omega = 0.011\Omega^*$ (or $f = 0.45$ THz.), $z_A = 7\,l^*$, $L = 14\,l^*$, $V_1 = 0.09$ V, and $N_{\rm SB} = 36$, we obtain $N_{\rm p}^{\rm s} = 0.02$.

Finally, we present in Fig. 6 the characteristics of $\Delta T_{RL}^{\rm s}$ along the $\mu = \Omega$ line for various ac potential field strength γU_1. To focus on the $\mu < \hbar\Omega$ regime, we have chosen a slightly larger $\hbar\Omega = \mu^+$. Our results show that as γ increases, or more sidebands are involved, the μ dependence of $\Delta T_{RL}^{\rm s}$ evolves from flat-out zero ($\gamma = 0$) to monotonic decreasing ($\gamma = 0.2$) to oscillatorylike (or nonmonotonic). Furthermore, the oscillatorylike characteristics (for $\gamma \geqslant 0.4$ in Fig. 6) have the number of $\Delta T_{RL}^{\rm s}$ undulations increasing with γ. This shows unequivocally that the nonmonotonic behavior in $\Delta T_{RL}^{\rm s}$, along Ω in Fig. 2, arises from large sideband processes.

In our calculations, we have included only the lowest subband for the QC. The subband energy spacing $\Delta\varepsilon$, when estimated by a hard wall of width $d = 5\,l^*$ (200 Å), gives $\Delta\varepsilon = 3(\pi/5)^2\hbar\Omega^* \approx 200$ meV. On the other hand, the ac SOI term that we have neglected is $\lambda V_1[\xi'(x,z_A) - \xi'(x,z_B)]\hbar\langle k_y\rangle$ where $\langle k_y\rangle$ is taken to be zero for intrasubband processes. For intersubband processes, we replace $\langle k_y\rangle \approx \pi/(5\,l^*)$ and, using the same pumping parameters in this work, we estimate the intersubband transition amplitude from the above ac SOI term (setting $x = 0$) to be of order 4 meV. This is much smaller than $\Delta\varepsilon$ and thus validates our one-subband treatment. Here, we have $|\xi'(0,z_A) - \xi'(0,z_B)| \approx 0.138/\,l^*$. We would also like to comment on the possible effect of Dresselhaus SOI (DSOI) on our results. The form of DSOI to be considered is $H_{\rm D}^0 = -\beta\langle k_z^2\rangle\sigma_x k_x$ [13], where for $\langle k_z^2\rangle \approx [\pi/(5\,l^*)]^2$ and $\beta = 761$ eV Å^3 gives us $H_{\rm D}^0 \approx -(0.187\,{\rm eV\,Å})\sigma_x k_x$. This could cause the rotation of the spin onto $\hat{z}$ in the presence of the ac SOI term in Eq. (9). However, from our other calculations (not shown) of including α_0, or $H_{\rm SO}^0$, into our spin pumping, we find its fractional contribution to be quite small, of order 5% of our spin-pumping results. As $H_{\rm SO}^0 = \hbar\alpha_0\,\sigma_y k_x \approx (0.523\,{\rm eV\,Å})\sigma_y k_x$, when an interface normal electric field of order $E_z \approx 10^5$ V/cm is assumed [37], it is larger than $H_{\rm D}^0$ magnitudewise. Thus, we reckon that the contribution from the $H_{\rm D}^0$, though differing in the spin directions, should be at best only of comparable order of magnitudes as that from $H_{\rm SO}^0$. As a result, the correction from DSOI is expected to be small.

V. CONCLUSION

Through this work, we come to realize that adiabatic spin pumping cannot be invoked by only one gate. It is obvious if the gate gives rise to only one ac field to the system. It cannot be invoked even when the gate gives rise to two ac fields, if the two fields differ only by a phase of either 0 or π [see Eq. (9)]. On the other hand, this work has firmly established that nonadiabatic spin pumping can be invoked by only one gate. This includes cases of one ac field, when a uniform static SOI is needed, and two ac fields, when a uniform static SOI is not needed. The key is the coherent sideband-processes nature of the nonadiabatic spin pumping.

It is worth putting our finite spin-pumping results in the perspectives of symmetry in our system. We focus on the two ac fields case ($\alpha_0 = 0$). The time-reversal symmetry (TRS) in Eq. (9) is clearly seen when we restore σ_y in place of η. Furthermore, the $x \to -x$ symmetry in the dimensionless field profile functions $f(x)$ and $g(x)$ [see Eqs. (10), (6), and (7)] leads to $T_{RL}^{\eta}(n) = T_{LR}^{\overline{\eta}}(n)$, and to Eq. (25). A consequence of Eq. (25) is that dc charge pumping is zero, as is expected for nonadiabatic pumping when both TRS and spatial symmetry are conserved [44]. On the other hand, for a given η, the SOI term (due to α_1) in Eq. (9) causes the breaking of the $x \to -x$ symmetry in H_η'. Since the other time-dependent term, namely, the $U_1 g(x)\cos(\Omega t)$ term, has the $x \to -x$ symmetry, thus we must have $T_{RL}^{\eta}(n) \neq T_{LR}^{\eta}(n)$ [44], or, summing over sidebands, to give

$$T_{RL}^{\eta} \neq T_{LR}^{\eta}. \tag{42}$$

The net pumped spin current $I_{\rm p}^{\rm s}$, given by

$$I_{\rm p}^{\rm s} = \frac{2}{h}\int_0^{\mu} dE[T_{RL}^{\uparrow} - T_{LR}^{\uparrow}], \tag{43}$$

is hence nonzero.

In conclusion, we have shown that significant spin pumping can be achieved in quantum channels with a single finger-gate capacitor. Resonant sideband processes are the major contributors to the spin pumping. Simultaneous couplings of the traversing electrons to both the ac SOI and ac potential fields provide the mechanisms to the spin pumping. Our perturbation theory has demonstrated clearly the physical mechanisms and the nonadiabatic nature for the spin pumping in this work. Our time-dependent scattering matrix approach provides an efficient numerical scheme for the calculations. The same spin-pumping mechanism holds also for a single finger gate, giving rise to smaller yet discernible spin-pumping results. These results should be of interest to the all-electric spin-pumping research, in particular, and to the spintronics research, in general.

ACKNOWLEDGMENT

This work was supported by Taiwan MOST (Contracts No. NSC 102-2112-M-009-005-MY3, No. NSC 102-2112-M-030-001-MY3, No. MOST 105-2112-M-009-008, No. MOST 105-2112-M-030-005), FJU Grant No. 3101311043504, and a MOE-ATU grant.

[1] I. Žutić, J. Fabian, and S. Das Sarma, Spintronics: Fundamentals and applications, Rev. Mod. Phys. **76**, 323 (2004).

[2] D. D. Awschalom, D. Loss, and N. Samarth, *Semiconductor Sprintronics and Quantum Computation* (Springer, Berlin, 2002).

[3] Y. Tserkovnyak, A. Brataas, G. E. W. Bauer, and B. I. Halperin, Nonlocal magnetization dynamics in ferromagnetic heterostructures, Rev. Mod. Phys. **77**, 1375 (2005).

[4] H. Nakayama, K. Ando, K. Harii, T. Yoshino, R. Takahashi, Y. Kajiwara, K. Uchida, and Y. Fujikawa, Geometry dependence on inverse spin Hall effect induced by spin pumping in $Ni_{81}Fe_{19}$/Pt films, Phys. Rev. B **85**, 144408 (2012).

[5] J.-C. Rojas-Sánchez, S. Oyarzún, Y. Fu, A. Marty, C. Vergnaud, S. Gambarelli, L. Vila, M. Jamet, Y. Ohtsubo, A. Taleb-Ibrahimi, P. Le Fèvre, F. Bertram, N. Reyren, J.-M. George, and A. Fert, Spin to Charge Conversion at Room Temperature by Spin

Pumping into a New Type of Topological Insulator: α-Sn Films, Phys. Rev. Lett. **116**, 096602 (2016).

[6] G. Schmidt, D. Ferrand, L. W. Molemkamp, A. T. Filip, and B. J. van Wees, Fundamental obstacle for electrical spin injection from a ferromagnetic metal into a diffusive semiconductor, Phys. Rev. B **62**, R4790 (2000).

[7] S. Sharma, A. Spiesser, S. P. Dash, S. Iba, S. Watanabe, B. J. van Wees, H. Saito, S. Yuasa, and R. Jansen, Anomalous scaling of spin accumulation in ferromagnetic tunnel devices with silicon and germanium, Phys. Rev. B **89**, 075301 (2014).

[8] R. M. Potok, J. A. Folk, C. M. Marcus, and V. Umansky, Detecting Spin-Polarized Currents in Ballistic Nanostructures, Phys. Rev. Lett. **89**, 266602 (2002).

[9] S. K. Watson, R. M. Potok, C. M. Marcus, and V. Umansky, Experimental Realization of a Quantum Spin Pump, Phys. Rev. Lett. **91**, 258301 (2003).

[10] S. M. Frolov, A. Venkatesan, W. Yu, J. A. Folk, and W. Wegscheider, Electrical Generation of Pure spin Currents in a Two-Dimensional Electron Gas, Phys. Rev. Lett. **102**, 116802 (2009).

[11] K. Hattori, Spin pumping from Rashba spin-orbit-coupled electron systems driven by electric dipole spin resonance, J. Phys. Soc. Jpn. **77**, 034707 (2008).

[12] A. F. Sadreev and E. Ya Sherman, Effect of gate-driven spin resonance on the conductance through a one-dimenaional quantum wire, Phys. Rev. B **88**, 115302 (2013).

[13] R. Winkler, *Spin-Orbit Coupling Effects in Two-Dimensional Electron and Hole Systems*, Springer Tracts in Modern Physics Vol. 191 (Springer, Berlin, 2003).

[14] M. Cardona, N. E. Christensen, and G. Fasol, Relativistic band structure and spin-orbit splitting of zinc-blende-type semiconductors, Phys. Rev. B **38**, 1806 (1988).

[15] R. L. Kallaher, J. J. Heremans, N. Goel, S. J. Chung, and M. B. Santos, Spin-orbit interaction determined by antilocalization in an InSb quantum well, Phys. Rev. B **81**, 075303 (2010).

[16] E. I. Rashba, Properties of semiconductors with an extremum loop. 1. Cyclotron and combinational resonance in a magnetic field perpendicular to the plane of the loop, Fizika tverd. Tela **2**, 1224 (1960) [Sov. Phys.–Solid State **2**, 1109 (1960)].

[17] Y. A. Bychkov and E. I. Rashba, Oscillatory effects and the magnetic susceptibility of carriers in inversion layers, J. Phys. C: Solid State Phys. **17**, 6039 (1984).

[18] P. Sharma and P. W. Brouwer, Mesoscopic Effects in Adiabatic Spin Pumping, Phys. Rev. Lett. **91**, 166801 (2003).

[19] M. Governale, F. Taddei, and R. Fazio, Pumping spin with electrical fields, Phys. Rev. B **68**, 155324 (2003).

[20] A. G. Mal'shukov, C. S. Tang, C. S. Chu, and K. A. Chao, Spin-current generation and detection in the presence of an ac gate, Phys. Rev. B **68**, 233307 (2003).

[21] L. Y. Wang, C. S. Tang, and C. S. Chu, Dc spin current generation in a Rashba-type quantum channel, Phys. Rev. B **73**, 085304 (2006).

[22] C. Li, Y. Yu, Y. Wei, and J. Wang, Nonadiabatic quantum spin pump: Interplay between spatial interference and photon-assisted tunneling in two-dimensional Rashba systems, Phys. Rev. B **75**, 035312 (2007).

[23] C. H. Lin, C. S. Tang, and Y. C. Chang, Nonmagnetic control of spin flow: generation of pure spin current in a Rashba-Dresselhaus quantum channel, Phys. Rev. B **78**, 245312 (2008).

[24] F. Liang, Y. H. Yang, and J. Wang, Electrical generation o pure spin current with oscillating spin-orbit interaction, Eur. Phys. J. B **69**, 337 (2009).

[25] P. Debray, S. M. S. Rahman, J. Wan, R. S. Newrock, M. Cahay, A. T. Ngo, S. E. Ulloa, S. T. Herbert, M. Muhammad, and M. Johnson, All-electric quantum point contact spin-polarizer, Nat. Nanotechnol. **4**, 759 (2009).

[26] Y. Avishai, D. Cohen, and N. Nagaosa, Purely Electric Spin Pumping in One Dimension, Phys. Rev. Lett. **104**, 196601 (2010).

[27] V. Brosco, M. Jerger, P. San-José, G. Zarand, A. Shnirman, and G. Schön, Prediction of resonant all-electric spin pumping with spin-orbit coupling, Phys. Rev. B **82**, 041309(R) (2010).

[28] D. Meidan, T. Micklitz, and P. W. Brouwer, Optimal topological spin pump, Phys. Rev. B **82**, 161303(R) (2010).

[29] S. Rojek, J. König, and A. Shnirman, Adiabatic pumping through an interacting quantum dot with spin-orbit coupling, Phys. Rev. B **87**, 075305 (2013).

[30] K. E. Nagaev and A. S. Goremykina, Charge and spin current in a quasi-one-dimensional quantum wire with spin-orbit coupling, Phys. Rev. B **89**, 035436 (2014).

[31] F. Nichele, S. Hennel, P. Pietsch, W. Wegscheider, P. Stano, P. Jacquod, T. Ihn, and K. Ensslin, Generation and Detection of Spin Currents in Semiconductor Nanostructures with Strong Spin-Orbit Interaction, Phys. Rev. Lett. **114**, 206601 (2015).

[32] J. Pawlowski, P. Szumniak, and S. Bednarek, Electron spin rotations induced by oscillating Rashba interaction in a quantum wire, Phys. Rev. B **93**, 045309 (2016).

[33] D. J. Thouless, Quantization of particle transport, Phys. Rev. B **27**, 6083 (1983).

[34] M. Büttiker, H. Thomas, and A. Prêtre, Current partition in multiprobe conductors in the presence of slowly oscillating external potentials, Z. Phys. B **94**, 133 (1994).

[35] P. W. Brouwer, Scattering approach to parametric pumping, Phys. Rev. B **58**, R10135 (1998).

[36] O. Entin-Wohlman and A. Aharony, Quantized adiabatic charge pumping and resonant transmission, Phys. Rev. B **66**, 035329 (2002).

[37] J. Nitta, T. Akazaki, H. Takayanagi, and T. Enoki, Gate Control of Spin-Orbit Interaction in an Inverted $In_{0.53}Ga_{0.47}As/In_{0.52}Al_{0.48}As$ Heterostructure, Phys. Rev. Lett. **78**, 1335 (1997).

[38] D. Grundler, Large Rashba Splitting in InAs Quantum Wells due to Electron Wave Function Penetration into the Barrier Layers, Phys. Rev. Lett. **84**, 6074 (2000).

[39] C. S. Tang and C. S. Chu, Coherent quantum transport in the presence of a finite-range transversely polarized time-dependent field, Phys. B (Amsterdam) **292**, 127 (2000).

[40] P. F. Bagwell and R. K. Lake, Resonances in transmission through an oscillatiing barrier, Phys. Rev. B **46**, 15329 (1992).

[41] C. S. Tang and C. S. Chu, Quantum Transport in the presence of a finite-range time-modulated potential, Phys. Rev. B **53**, 4838 (1996).

[42] J. H. Davies, I. A. Larkin, and E. V. Sukhorukov, Modeling the patterned two-dimensional electron gas: Electrostatics, J. Appl. Phys. **77**, 4504 (1995).

[43] M. Büttiker, Four-Terminal Phase-Coherent Conductance, Phys. Rev. Lett. **57**, 1761 (1986).

[44] M. Moskalets and M. Büttiker, Floquet scattering theory of quantum pumps, Phys. Rev. B **66**, 205320 (2002).